

Measuring patchy reionisation with kSZ²-21 cm correlations

Q. Ma^{1,2,6,*}, K. Helgason^{2,3}, E. Komatsu^{2,5}, B. Ciardi², A. Ferrara^{4,5}

¹ Purple Mountain Observatory, Chinese Academy of Sciences, Nanjing 210008, China

² Max-Planck-Institut für Astrophysik, Karl-Schwarzschild-Straße 1, D-85748 Garching bei München, Germany

³ Centre for Astrophysics and Cosmology, University of Iceland, Dunhagi 5, 107 Reykjavík, Iceland

⁴ Scuola Normale Superiore, Piazza dei Cavalieri 7, I-56126 Pisa, Italy

⁵ Kavli Institute for the Physics and Mathematics of the Universe (Kavli IPMU, WPI), Todai Institutes for Advanced Study, University of Tokyo, Kashiwa 277-8583, Japan

⁶ University of Chinese Academy of Sciences, Beijing 100049, China

Accepted XXX. Received YYY; in original form ZZZ

ABSTRACT

We study cross-correlations of the kinetic Sunyaev-Zel’dovich effect (kSZ) and 21 cm signals during the epoch of reionisation (EoR) to measure the effects of patchy reionisation. Since the kSZ effect is proportional to the line-of-sight velocity, the kSZ-21 cm cross correlation suffers from cancellation at small angular scales. We thus focus on the correlation between the kSZ-squared field (kSZ²) and 21 cm signals. When the global ionisation fraction is low ($x_e \lesssim 0.7$), the kSZ² fluctuation is dominated by rare ionised bubbles which leads to an anti-correlation with the 21 cm signal. When $0.8 \lesssim x_e < 1$, the correlation is dominated by small pockets of neutral regions, leading to a positive correlation. However, at very high redshifts when $x_e < 0.15$, the spin temperature fluctuations change the sign of the correlation from negative to positive, as weakly ionised regions can have strong 21 cm signals in this case. To extract this correlation, we find that Wiener filtering is effective in removing large signals from the primary CMB anisotropy. The expected signal-to-noise ratios for a ~ 10 -hour integration of upcoming Square Kilometer Array data cross-correlated with maps from the current generation of CMB observatories with $3.4 \mu\text{K arcmin}$ noise and 1.7 arcmin beam over 100 deg^2 are 51, 60, and 37 for $x_e = 0.2, 0.5,$ and 0.9 , respectively.

Key words: cosmology: cosmic background radiation – reionisation – early Universe

1 INTRODUCTION

The kinetic Sunyaev-Zel’dovich (kSZ) effect (Sunyaev & Zeldovich 1980) is a powerful probe of the physics of the epoch of reionisation (EoR), as it is sensitive to patchiness of ionised bubbles (see Park et al. 2013, and references therein). Measurements of the power spectrum of the kSZ, however, face two challenges. First, we can only measure the sum of the kSZ power spectra from the EoR and post EoR, and the latter is larger than the former by at least a factor of two (e.g., Shaw et al. 2012; Park et al. 2016). Second, the kSZ power spectrum is sub-dominant compared to other components including the primary cosmic microwave background (CMB) temperature anisotropy, foreground sources, and the thermal Sunyaev-Zel’dovich effect (George et al. 2015), and thus inaccurate modeling

of these components results in inaccurate estimation of the kSZ power spectrum.

These issues arise because we have no redshift information of the kSZ. Cross-correlating the kSZ with 21 cm fluctuations from neutral hydrogen atoms would allow us to do “tomography” of the kSZ as a function of redshift because the frequencies of measured 21 cm lines can be translated into z (Alvarez et al. 2006; Adshead & Furlanetto 2008; Alvarez 2016). This cross-correlation not only helps measurements of the kSZ from the EoR, but also 21 cm signals, as the latter are contaminated by the Galactic and extragalactic foreground emission and instrumental systematics arising from, e.g., miscalibration of gains, polarisation-to-intensity leakages, etc (Patil et al. 2017), which are not correlated with the CMB data¹.

In this paper we use semi-numerical simulations of the

* E-mail: maqb@mpa-garching.mpg.de

¹ There is still a possibility that unresolved radio sources have both the 21 cm and CMB data that can correlate.

EoR (Mesinger et al. 2011) to study the cross-correlation between kSZ and 21 cm signals. In particular, we investigate the cross-correlation between *squared* kSZ fluctuations and 21 cm signals. This was considered in the context of cross-correlation with weak lensing by the large-scale structure (Doré et al. 2004), as well as with galaxies (Hill et al. 2016; Ferraro et al. 2016) in a low redshift universe. This approach works better because it avoids line-of-sight cancellation of the kSZ-density correlation.

The rest of the paper is organised as follows. We describe our simulations in section 2. In section 3 we first test the fidelity of our simulated kSZ maps by using the kSZ auto power spectrum, and then show that the kSZ-21 cm correlation suffers from line-of-sight cancellation on small angular scales. We then present our results for the kSZ²-21 cm correlations. In section 4 we discuss the detectability of the kSZ²-21 cm correlations from the EoR by calculating signal-to-noise ratios of some representative experimental configurations. We conclude in section 5.

Throughout this paper we use the best-fitting cosmological parameters from *Planck*+WP+highL+BAO data (Planck Collaboration et al. 2014): cosmological constant $\Omega_\Lambda = 0.6914$, matter density $\Omega_M = 0.3086$, baryon matter density $\Omega_b = 0.0483$, scalar spectral index $n_s = 0.9611$, matter fluctuation amplitude $\sigma_8 = 0.8288$, and Hubble constant $H_0 = 67.77$ Km/s/Mpc ($h = 0.6777$).

2 SIMULATIONS

Temperature anisotropy due to the kSZ effect is given by (Sunyaev & Zeldovich 1980):

$$\delta T_{\text{kSZ}}(\hat{\gamma}) = -T_0 \int d\tau e^{-\tau} \frac{\hat{\gamma} \cdot \mathbf{v}}{c}, \quad (1)$$

where $T_0 = 2.728$ K is the CMB temperature at $z = 0$, c the speed of light, \mathbf{v} the bulk peculiar velocity of ionised gas, $\hat{\gamma}$ a unit vector of the line-of-sight (LOS), and τ the optical depth of free electron scattering, i.e.,

$$d\tau = \sigma_T N_{b,0} (1+z)^2 (1+\delta) x_e ds, \quad (2)$$

where σ_T is the Thomson scattering cross-section, $N_{b,0} = 0.2 (\Omega_b h^2 / 0.022) \text{ m}^{-3}$ the average atomic number density at $z = 0$, δ the matter overdensity, x_e the ionisation fraction (assuming the same ionisation fraction for HI and HeI and no HeII ionised during the EoR), $ds = c/H(z) dz$ the differential comoving distance s , and $H(z) = H_0 \sqrt{\Omega_M (1+z)^3 + \Omega_\Lambda}$ the Hubble expansion rate at z .

As $\tau = \int_0^z d\tau$ is usually much smaller than unity, we shall ignore fluctuations in $e^{-\tau} \approx 1 - \tau$. Then the kSZ is determined by a specific ionised momentum field defined by $\mathbf{q} \equiv x_e (1 + \delta) \mathbf{v}$.

The offset of the 21 cm brightness temperature from the CMB, $\delta T_{21\text{cm}}$, is expressed as (Mesinger et al. 2011):

$$\delta T_{21\text{cm}} = \Psi_{21\text{cm}} (1-x_e) (1+\delta) \left(\frac{H}{dv_s/ds + H} \right) \left[1 - \frac{T_0 (1+z)}{T_S} \right], \quad (3)$$

where $\Psi_{21\text{cm}} \approx 27 \text{ mK} [(1+z)/10]^{1/2}$, dv_s/ds is a gradient of the comoving velocity along the LOS, and T_S is the gas spin temperature. As in this paper we are only considering

the 21 cm signals perpendicular to the LOS, we ignore the redshift space distortion term, dv_s/ds , in the denominator.

We use the semi-numerical simulation code 21cmFAST (Mesinger et al. 2011) to calculate the ionisation fraction, matter density, and peculiar velocity fields. The simulations start at $z = 30$ with a box of comoving 2000 Mpc per side and a grid of 400^3 cells. This gives a resolution of 5 Mpc per cell. The volume of the box is large enough to encompass the redshift range from $z = 20$ to $z = 7.5$, where we save outputs. We integrate Eq. 1 in each resolution element through the box to obtain 2-D kSZ maps (see left panel of Fig. 1), by using the plane-parallel approximation instead of tracing the actual LOS. 21cmFAST also provides the 21 cm field, as shown in the middle panel of Fig. 1.

Regarding the ionisation processes, 21cmFAST keeps track of both UV and X-ray radiation, i.e. a cell is ionised if $\zeta_{\text{UV}} f_{\text{coll}}(R) \geq 1 - x_{e,X}$, where f_{coll} is the collapsed fraction inside a sphere with a radius R , ζ_{UV} is the ionising efficiency factor of UV photons, and $x_{e,X}$ is the fraction ionised by X-ray radiation (for details, see Mesinger et al. 2013). The X-ray emission is due to stellar remnants, e.g. X-ray binaries whose ionising efficiency factor is related to the star formation, $\zeta_X = (N_X / 10^{56} \text{ M}_\odot) (f_*/0.1)$, where N_X is the X-ray (≥ 0.3 KeV) photon number emitted per solar mass during the whole life of stars (in units of M_\odot^{-1}), and f_* is the fraction of collapsed baryons converted into stars (Mesinger et al. 2013). The values we adopted for these parameters are $\zeta_{\text{UV}} = 31.5$ and $\zeta_X = 1$.

We generate 20 realisations to obtain good statistics. Each realisation gives three independent 2-D kSZ maps along three axes of the snapshot; thus, we have 60 realisations of kSZ maps and the corresponding 21 cm fields.

The right panel of Fig. 1 shows the reionisation history of our simulations. The reionisation completes at $z \approx 8$, with half-ionisation at $z = 10.8$. Assuming that hydrogen is fully ionised at $z < 8$ and helium is singly ionised ($x_{\text{HeII}} = 1$) at $z > 3$ and doubly ionised ($x_{\text{HeIII}} = 1$) at $z < 3$, we obtain an optical depth of $\tau \approx 0.0996$, which is high compared to the latest determination by Planck (Planck Collaboration et al. 2016).

The left panel of Fig. 1 shows one realisation of the kSZ map, while the middle panel shows a slice of the 21 cm brightness temperature at $z = 10.8$ ($x_e = 0.5$). The kSZ signal is primarily generated by a long-wavelength peculiar velocity field modulated by small-scale electron density fluctuations (Hu 2000). This is the reason that the kSZ map is dominated visually by long-wavelength modes.

3 ANGULAR POWER SPECTRA

In the flat-sky approximation, the angular spectrum is computed by

$$\langle \tilde{X}^*(\mathbf{l}) \tilde{Z}(\mathbf{l}') \rangle = C_{X-Z}(l) \delta_{\text{D}}(\mathbf{l} - \mathbf{l}'), \quad (4)$$

where δ_{D} is the Dirac delta function, X and Z are maps, and \tilde{X} and \tilde{Z} are their Fourier transforms:

$$\tilde{X}(\mathbf{l}) = \frac{1}{2\pi} \int d^2 \hat{\gamma} X(\hat{\gamma}) e^{-i\mathbf{l} \cdot \hat{\gamma}}. \quad (5)$$

If $X = Z$, $C_{X-X}(l)$ is the auto power spectrum of a 2-D map X .

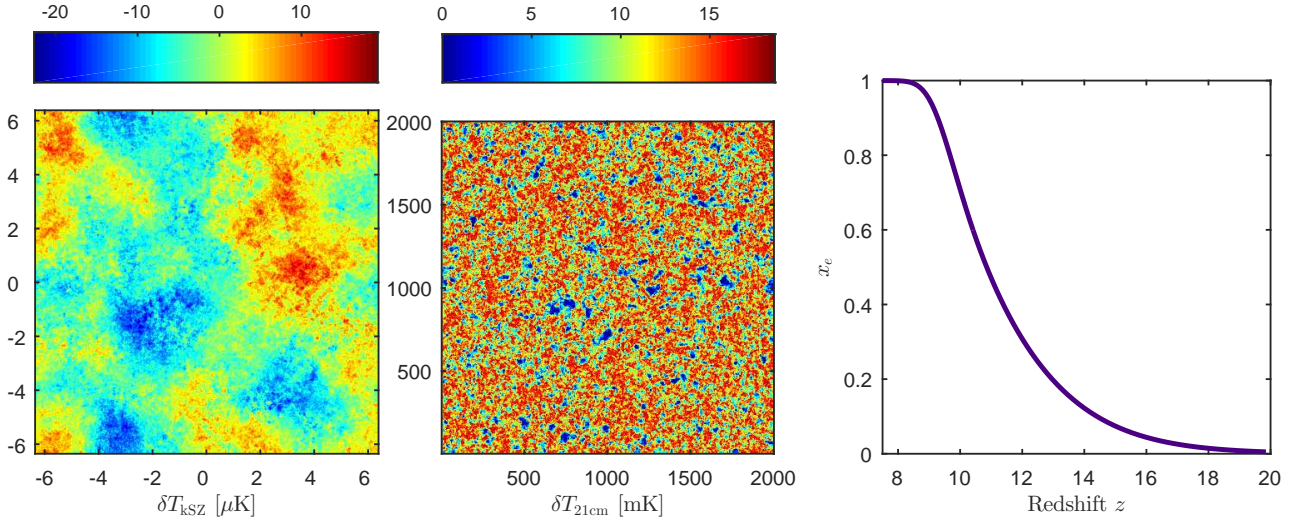


Figure 1. **Left panel:** One realisation of kSZ map (δT_{kSZ} in units μK). The size of the map is approximately $12.7^\circ \times 12.7^\circ$. **Middle panel:** A slice of 21 cm brightness temperature ($\delta T_{21\text{cm}}$ in units mK) at $x_e = 0.5$ ($z = 10.8$). The physical linear size of this map is 2000 comoving Mpc. **Right panel:** Reionisation history (x_e) as a function of redshift.

3.1 kSZ auto power spectrum

In the top panel of Fig. 2, we show the kSZ auto power spectrum with the error bars on the average derived from 60 realisations.

To check the fidelity of the maps, we also compute the kSZ power spectrum by directly integrating the 3-D power spectra of specific momentum fields over redshifts. The momentum fields consist of two components: the transverse mode whose direction is perpendicular to the wavenumber, \mathbf{k} , i.e., $\mathbf{k} \perp \mathbf{q}_\perp$, and the longitudinal mode, $\mathbf{k} \parallel \mathbf{q}_\parallel$. Using Limber’s approximation (Limber 1953), we obtain (Park et al. 2013; Alvarez 2016)

$$C_{\mathbf{q}_\perp}(l) = \left(\frac{\sigma_T N_{b,0} T_0}{c} \right)^2 \int (1+z)^4 \frac{ds}{s^2} e^{-2\tau} \frac{P_{\mathbf{q}_\perp}(l/s, z)}{2} \quad (6)$$

$$C_{\mathbf{q}_\parallel}(l) = \frac{1}{l^2} \int ds \Psi_\parallel^2 \frac{P_{\delta\delta}(l/s, z)}{(l/s)^2}, \quad (7)$$

where in the last line we have used linear theory to relate the longitudinal velocity with the matter density. Here, $P_{\delta\delta}$ is the power spectrum of matter density, $\Psi_\parallel \equiv \frac{T_0}{cD} d(a\dot{D} \frac{d\tau}{ds})/ds$, D is the growth factor of linear matter density fluctuations, and \dot{D} is the time derivative of $D(z)$. We evaluate these integrals using $P_{\mathbf{q}_\perp}$ and $P_{\delta\delta}$ measured from the simulations.

The factor of l^{-2} in Eq. 7 is a consequence of LOS cancellation; namely, the kSZ is caused by the LOS component of velocities, and the longitudinal velocities are parallel to \mathbf{k} . As the longitudinal modes change signs along the LOS, short wavelength modes suffer from cancellations (Vishniac 1987). Therefore, the longitudinal modes dominate at large angular scales.

We find that the Limber formula agrees well with the kSZ power spectrum measured from the maps at $l \gtrsim 10^3$. However, at much lower multipoles, the power measured from the maps is substantially larger than the Limber formula for the longitudinal mode. This large-scale mismatch originates from boundary effects as the LOS cancellation

does not occur at the near/far boundaries of our lightcone (i.e. at $z \sim 7.5$ and $z \sim 20$).

3.2 kSZ-21 cm correlation

The middle panel of Fig. 2 shows the cross power spectra of kSZ with 21 cm at $x_e = 0.2, 0.5$ and 0.9 , together with the results from the Limber formula (Alvarez et al. 2006)²:

$$C_{\text{kSZ}-21\text{cm}}(l) = \frac{1}{l^2} \Psi_\parallel \Psi_{21\text{cm}} \kappa \left\{ -x_e P_{\delta\delta_x} \left(\frac{l}{s}, z \right) + (1-x_e) \left[P_{\delta\delta} \left(\frac{l}{s}, z \right) + P_{\delta\delta_\kappa} \left(\frac{l}{s}, z \right) \right] \right\}, \quad (8)$$

where $\kappa \equiv 1 - T_0(1+z)/T_S$, $P_{\delta\delta_x}$ is the cross power spectrum of matter density and ionisation fraction fluctuations, and $P_{\delta\delta_\kappa}$ is the cross power spectrum of matter density and κ fluctuations.

Here, the factor l^{-2} is again due to LOS cancellation, as the correlation is dominated by the longitudinal modes correlated with density fields. The correlation between the transverse modes and density fields involves a three-point correlation of $(\mathbf{v}\delta)_\perp \delta$, which vanishes for Gaussian fluctuations. We evaluate Eq. 8 using all the 3-D power spectra measured from the simulations. We find excellent agreement between the power spectra measured from maps and the Limber results, which indicates that the contribution from the transverse modes is indeed negligible.

In the top panel of Fig. 3 we show the redshift evolution of the kSZ-21 cm cross power spectrum at $l = 100$ and 500 together with the Limber results. Because the correlations are overestimated at the lightcone boundaries, we crop the evolution to $z = 16.7 - 8.5$. Our results are in agreement with Alvarez et al. (2006), apart from high redshifts where the

² We have added a term including spin temperature T_S , while when $T_S \gg T_{\text{CMB}}$, Eq. 8 can be simplified to the Eq. 17 in Alvarez et al. (2006).

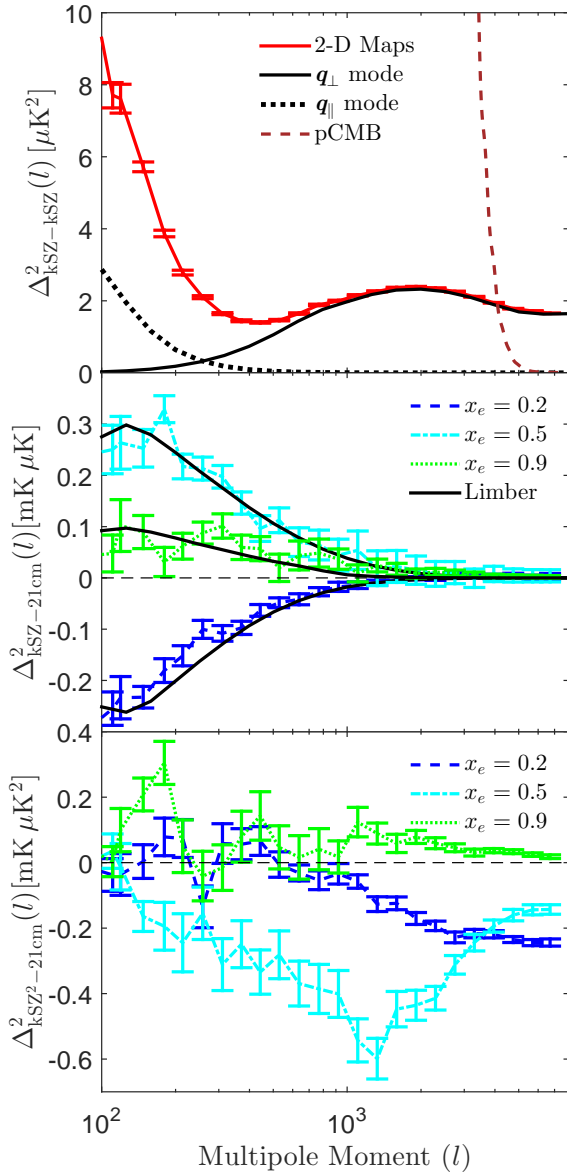


Figure 2. **Top panel:** kSZ auto power spectrum, $\Delta^2(l) = l(l+1)C(l)/2\pi$, averaged over 60 realisations (solid red line). The error bars are the errors on the average (i.e., r.m.s. scatter divided by $\sqrt{60}$). The solid (dotted) black line shows the power spectrum of transverse (longitudinal) momentum derived from the 3-D power spectra integrated over redshifts using Limber’s approximation. The dashed line shows the primary CMB power spectrum. **Middle panel:** kSZ-21 cm cross power spectra at $x_e = 0.2$ ($z = 13$; dashed blue), $x_e = 0.5$ ($z = 10.8$; dash-dotted cyan), and $x_e = 0.9$ ($z = 9.3$; dotted green). The solid black lines are the corresponding Limber results. The horizontal dashed line shows zero. **Bottom panel:** Same as the middle panel but for kSZ^2 -21 cm cross correlations.

spin temperature makes the cross-correlation more negative. This happens because T_S strongly correlates with the matter density, i.e., $P_{\delta\delta_\kappa} \gg P_{\delta\delta}$, the magnitude of the kSZ-21 cm correlation becomes larger as z increases.

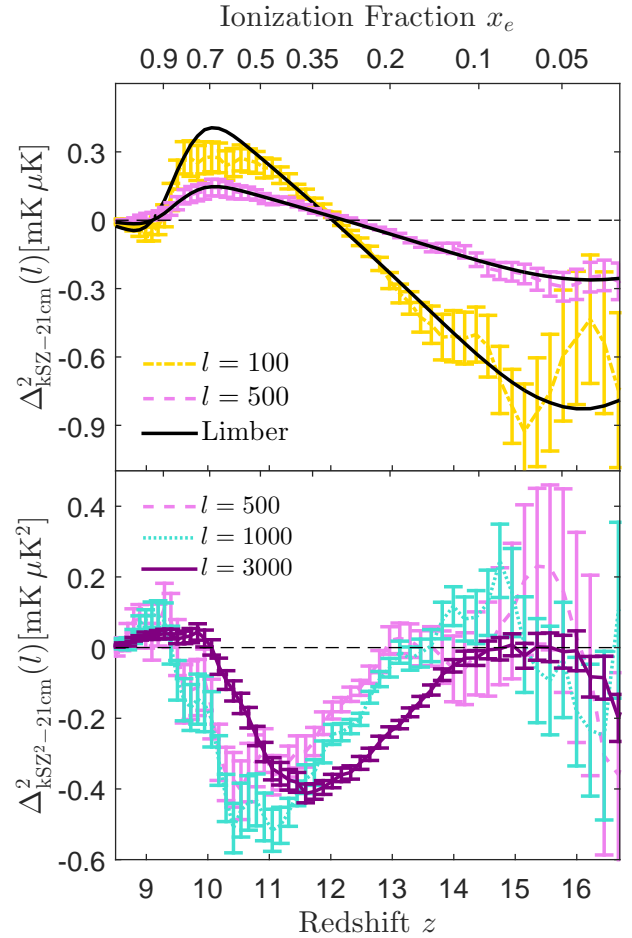


Figure 3. **Top panel:** Redshift evolution of the kSZ-21 cm cross power spectra at $l = 100$ (dash-dotted yellow) and 500 (dashed violet). The black lines are the corresponding Limber results. The horizontal dashed line shows zero. **Bottom panel:** Same as the top panel but for kSZ^2 -21 cm cross correlations of $l = 500$, 1000, and 3000.

3.3 kSZ^2 -21 cm correlation

In order to detect the cross-correlation between kSZ and 21 cm signals, we need to overcome the LOS cancellation. One way to achieve this is to cross-correlate *squared* kSZ fields with density fields (Doré et al. 2004). Then the correlation between kSZ^2 and 21 cm signals would persist at small angular scales.

To avoid the contamination of boundary effects at large scales, we remove the kSZ signals at $l < 100$ before squaring, and only focus on the correlations at $z = 16.7 - 8.5$ and $l > 100$.

In the bottom panel of Fig. 2 we show the kSZ^2 -21 cm cross power spectra at $x_e = 0.2, 0.5$ and 0.9 as a function of multipoles with the error bars on the average of 60 realisations, while in the bottom panel of Fig. 3 we show redshift evolution of the spectra at $l = 500, 1000$, and 3000 . These spectra evolve rapidly with ionisation fraction. For example, at $x_e = 0.2$ ($z = 13$) kSZ^2 correlates negatively with the 21 cm signal at small scales ($l > 10^3$), but no significant correlations are visible at large scales ($l < 10^3$), whereas at $x_e = 0.5$ ($z = 10.8$) the kSZ^2 -21 cm correlation is negative in the entire multipole range. At a later stage of reionisa-

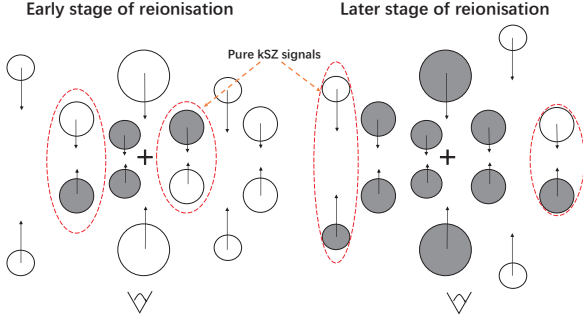


Figure 4. Simplified diagram to illustrate the dependence of kSZ^2 fluctuations on the reionisation phase, assuming the velocities along LOS appear as pairs. During the early stages of reionisation (left), when the Universe is lowly ionised, the ionised bubbles (gray) have a larger probability to meet neutral pair partners (white) than ionised ones and then remain pure kSZ signals (embedded in red dashed lines). In this case, the kSZ^2 fluctuations are dominated by the ionised bubbles. At a later stage of reionisation (right), when the Universe is highly ionised, the situation is reversed and the neutral regions have a higher probability to remain pure kSZ signals compared to the ionised bubbles. The kSZ^2 fluctuations are thus dominated by the neutral regions.

tion, when $x_e = 0.9$ ($z = 9.3$), the correlation turns slightly positive.

The evolution of kSZ^2 -21 cm cross power spectra can be understood in terms of the highly non-Gaussian nature of reionisation. When ionisation is low, e.g. at $x_e < 0.7$ ($z > 10$), the kSZ^2 -21 correlation is dominated by rare ionised bubbles (see the left part of illustration in Fig. 4) that anti-correlate with the 21 cm signal arising from the neutral medium, resulting in negative cross spectra.

On the other hand, kSZ^2 shows positive correlations with 21 cm at $x_e < 0.15$ ($z > 14$), when the spin temperature dominates the 21 cm signal. This is because T_S correlates strongly with the matter density at these epochs.

When the Universe is highly ionised, e.g. at $x_e > 0.8$ ($z < 9.7$), kSZ^2 fluctuations are dominated by the small remains of the neutral medium (see the right part of illustration in Fig. 4), resulting in positive cross spectra with 21 cm signals.

4 SIGNAL-TO-NOISE RATIO

We calculate the expected signal-to-noise ratios (S/N) of the kSZ^2 -21 cm correlations. We adopt specifications similar to those of LOFAR (Vrbanec et al. 2016) and SKA (Koopmans et al. 2015) for 21 cm observations, and those of the current generation of ground-based CMB observatories such as SPT-3G (Benson et al. 2014) and Advanced ACT (Henderson et al. 2016).

We estimate the S/N per multipole bin as (Doré et al. 2004)

$$\left(\frac{S}{N}\right)^2 = \frac{f_{\text{sky}}(2l+1)l_{\text{bin}}C_{kSZ^2,21\text{cm}}^2}{C_{\text{CMB}^2}(C_{21\text{cm}} + N_{21\text{cm}}) + C_{kSZ^2,21\text{cm}}^2}, \quad (9)$$

where $l_{\text{bin}} \approx 0.46l$ ($(\log_{10}l)_{\text{bin}} = 0.2$) is the bin width at a given l , f_{sky} the fraction of sky observed by both CMB and

Experiment	θ_{FWHM}	$\sigma_{\text{pix}}(\mu\text{K})$	f_{sky}
CMB	1.7	2	0.0024
LOFAR	3.5	76×10^3	0.0006
SKA	1.0	10×10^3	0.0024

Table 1. Characteristics of CMB and 21 cm experiments.

21 cm experiments, C_{CMB^2} the power spectrum of CMB-squared, and $C_{21\text{cm}}$ and $N_{21\text{cm}}$ are the auto spectrum of the 21 cm signal and its noise, respectively.

In the CMB maps we include primary CMB and the thermal SZ effect (Dolag et al. 2016). To this we also add the Poisson and clustered power from dusty star-forming galaxies and the Poisson power from radio galaxies, for which we use the values estimated by the SPT Collaboration (George et al. 2015). Finally we add Gaussian, white instrumental noise of $3.4 \mu\text{K arcmin}$ which corresponds to a noise per pixel of $\sigma_{\text{pix}} = 2 \mu\text{K}$ with our pixel size of 1.7 arcmin. We then use these maps to calculate C_{CMB^2} in Eq. 9.

The auto spectra of 21 cm signals, $C_{21\text{cm}}$, come from our simulations, and the noise power is given by $N_{21\text{cm}} = [(1+z)/9.5]^2 \sigma_{\text{pix}}^2 \theta_{\text{FWHM}}^2$ (Doré et al. 2004). We adopt $\theta_{\text{FWHM}} = 3.5$ arcmin and $\sigma_{\text{pix}} = 76$ mK at 150 MHz ($z \approx 8.5$) for LOFAR (Vrbanec et al. 2016), assuming 600 hours of integration and a bandwidth of 0.5 MHz. SKA will have a superior angular resolution of $\theta_{\text{FWHM}} = 1$ arcmin (Koopmans et al. 2015), and a lower noise level. We adopt $\sigma_{\text{pix}} = 10$ mK at 150 MHz, which corresponds to ~ 10 hours of integration and 1 MHz of bandwidth.

Finally, we assume that both CMB and 21 cm experiments will have an overlapping region of 100 deg^2 ($f_{\text{sky}} = 0.0024$) for SKA, and 25 deg^2 for LOFAR. These parameters are listed in Table 4.

Note that both squared fields and 21 cm signals are non-Gaussian, but Eq. 9 is valid only for Gaussian fields. Thus, the S/N estimate given here is only approximate.

We find that the S/N is small ($\ll 1$) for any combinations of CMB and 21 cm experiments, mainly because of the large noise from the primary CMB signal. To mitigate this problem, in the next section we apply the commonly adopted Wiener filtering (Doré et al. 2004).

4.1 Wiener filtering

To suppress primary CMB “noise”, we apply the following filter (Doré et al. 2004; Hill et al. 2016; Ferraro et al. 2016)

$$F(l) = \frac{C_{kSZ}(l)}{C_{kSZ}(l) + C_{\text{pCMB}}(l) + C_{\text{fore}}(l)}, \quad (10)$$

where C_{pCMB} is the primary CMB power spectrum, and C_{fore} is the sum of the foreground terms including the thermal SZ, dusty star-forming galaxies and radio galaxies. As Wiener filtering will automatically suppress low l power, we do not crop the CMB fluctuations at $l < 100$ before applying the filtering.

In Fig. 5 we show the predicted S/N as a function of multipoles at $x_e = 0.2, 0.5$ and 0.9 after filtering. We find that the S/N for LOFAR is always below 5. SKA though is much more promising, having a S/N per multiple bin > 10

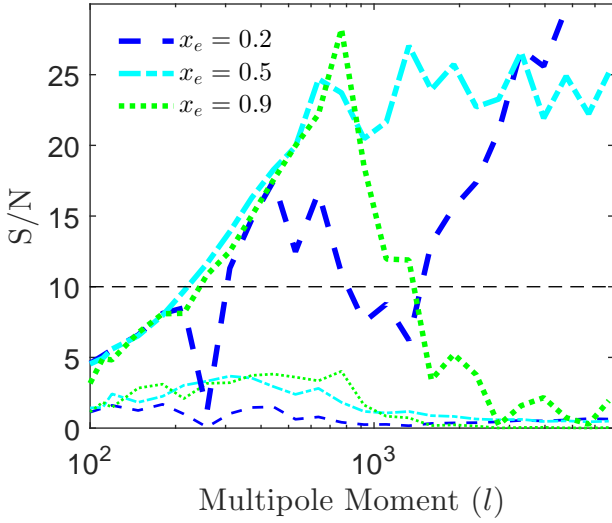


Figure 5. Predicted S/N of the kSZ²-21 cm correlations per multipole bin after Wiener filtering for $x_e = 0.2$ ($z = 13$; dashed blue), $x_e = 0.5$ ($z = 10.8$; dash-dotted cyan), and $x_e = 0.9$ ($z = 9.3$; dotted green). The thick and thin lines refer to the SKA and LOFAR case, respectively. The horizontal line marks S/N = 10.

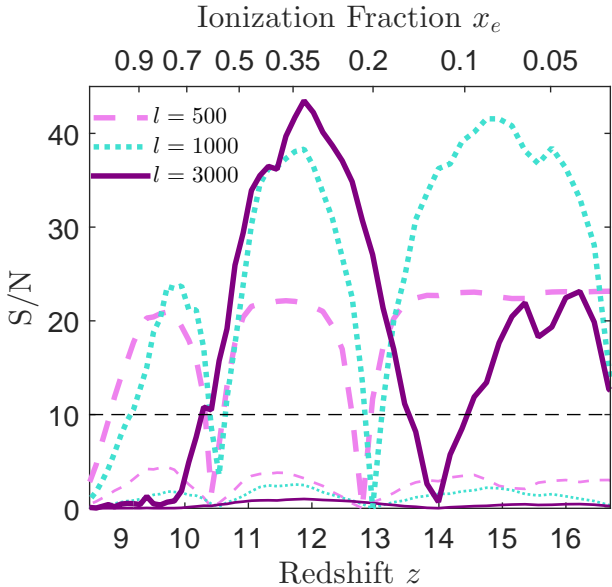


Figure 6. Predicted S/N of the kSZ²-21 cm correlations after Wiener filtering as a function of redshift for multipole bins of $l = 500$ (dashed violet), 1000 (dotted turquoise), and 3000 (solid purple). The thick and thin lines refer to the SKA and LOFAR case, respectively. The horizontal line shows S/N = 10.

at $x_e = 0.9$ in the range $l = 200 - 1000$, at $x_e = 0.5$ for $l > 200$, and at $x_e = 0.2$ for $l \sim 400$ and $l > 2000$.

In Fig. 6 we show the S/N as a function of redshift for $l = 500, 1000$ and 3000 . SKA is expected to have a S/N > 10 over a wide redshift range, except two narrow gaps at $z \sim 10.5$ ($x_e \sim 0.6$) and $z \sim 13$ ($x_e \sim 0.2$), where the correlations are very weak (see the bottom panel of Fig. 3).

To obtain the total S/N rather than the S/N per mul-

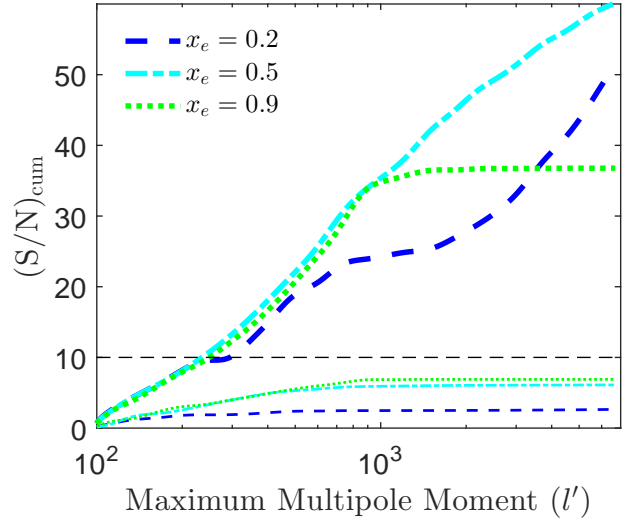


Figure 7. Cumulative S/N as a function of the maximum multipole. The meaning of the lines is the same as that in Fig. 5.

tipole bin, we compute the cumulative S/N as

$$\left(\frac{S}{N}\right)_{\text{cum}}^2 (< l') = \sum_i \frac{f_{\text{sky}}(2l_i + 1)\Delta l_i C_{\text{kSZ}^2, 21\text{cm}}^2}{C_{\text{CMB}}^2(C_{21\text{cm}} + N_{21\text{cm}}) + C_{\text{kSZ}^2, 21\text{cm}}^2}, \quad (11)$$

where i denotes the i th bin, and l_i is the central multipole of the i th bin with bin width Δl_i . We display it in Fig. 7 as a function of the maximum multipole l' . The cumulative S/N for LOFAR is < 10 , while the SKA would have S/N as large as 51.4, 60.2, and 36.8 at $x_e = 0.2, 0.5$ and 0.9 , respectively.

5 CONCLUSIONS AND DISCUSSION

We have used the semi-numerical 21cmFAST simulations (Mesinger et al. 2011) to study cross-correlations of the kSZ and 21 cm signals from the EoR. As the kSZ-21 cm correlation suffers from the line-of-sight cancellation at small angular scales, we have focused on the cross-correlation between squared kSZ fields and 21 cm signals. We find that the line-of-sight cancellation is mitigated and the cross-correlation persists at small angular scales.

The goal of this work is to capture the general behavior of the kSZ²-21 cm cross-correlation signal. We caution that the simplified scheme of 21cmFAST may not be adequate to quantify the signal in detail, and one may need more sophisticated reionisation simulations (e.g. Park et al. 2013). It is also important to acknowledge that we have performed our calculations only for one specific set of cosmological parameters and reionisation history; thus, we have not investigated how the predicted signals change when we change the physics of reionisation. In particular, the optical depth from the latest Planck data (Planck Collaboration et al. 2016) ($\tau = 0.058 \pm 0.012$) is lower than that from our simulation ($\tau \approx 0.1$), and its impact is not obvious. Finally, we neglected any correlation between foregrounds in 21 cm and kSZ maps which, if present, would contaminate the reionisation signal. The contribution from foregrounds, such as continuum radio sources, would merit further study as well.

The kSZ^2 -21 cm cross-correlation signal exhibits interesting features, such as a sign change according to phases of reionisation. For example, the correlation is positive for ionisation fraction $x_e < 0.15$ (when density fluctuations dominate the 21 cm signal) and at $x_e > 0.8$ (when the Universe is highly ionised), while it is negative for intermediate ionisation fractions. Thus, not only is the cross-correlation powerful for minimising the foreground emission and instrumental systematics of either kSZ or 21 cm data, but also it offers a powerful probe of reionisation.

In general, prospects for measuring the kSZ^2 -21 cm cross-correlation signal are good: SKA cross-correlated with on-going CMB experiments such as SPT-3G and Advanced ACT should yield high signal-to-noise ratio measurements of the cross-correlation over a wide range of multipoles and redshifts.

ACKNOWLEDGMENTS

We acknowledge the helpful discussions with V. Jelic and M. Alvarez. The tools for bibliographic research are offered by the NASA Astrophysics Data Systems and by the JSTOR archive. QM is supported by the National Natural Science Foundation of China (Grant Nos 11373068 and 11322328), the National Basic Research Program (973 Program) of China (Grant Nos 2014CB845800 and 2013CB834900) and the Strategic Priority Research Program The Emergence of Cosmological Structures (Grant No. XDB09000000) of the Chinese Academy of Sciences. EK is supported in part by JSPS KAKENHI Grant Number JP15H05896. KH acknowledges support from the Icelandic Research Fund, Grant Number 173728-051.

References

- Adshhead P. J., Furlanetto S. R., 2008, *MNRAS*, **384**, 291
 Alvarez M. A., 2016, *ApJ*, **824**, 118
 Alvarez M. A., Komatsu E., Doré O., Shapiro P. R., 2006, *ApJ*, **647**, 840
 Benson B. A., et al., 2014, in Millimeter, Submillimeter, and Far-Infrared Detectors and Instrumentation for Astronomy VII. p. 91531P ([arXiv:1407.2973](https://arxiv.org/abs/1407.2973)), doi:10.1117/12.2057305
 Dolag K., Komatsu E., Sunyaev R., 2016, *MNRAS*, **463**, 1797
 Doré O., Hennawi J. F., Spergel D. N., 2004, *ApJ*, **606**, 46
 Ferraro S., Hill J. C., Battaglia N., Liu J., Spergel D. N., 2016, *Phys. Rev. D*, **94**, 123526
 George E. M., et al., 2015, *ApJ*, **799**, 177
 Henderson S. W., et al., 2016, *Journal of Low Temperature Physics*, **184**, 772
 Hill J. C., Ferraro S., Battaglia N., Liu J., Spergel D. N., 2016, *Physical Review Letters*, **117**, 051301
 Hu W., 2000, *ApJ*, **529**, 12
 Koopmans L., et al., 2015, Advancing Astrophysics with the Square Kilometre Array (AASKA14), p. 1
 Limber D. N., 1953, *ApJ*, **117**, 134
 Mesinger A., Furlanetto S., Cen R., 2011, *MNRAS*, **411**, 955
 Mesinger A., Ferrara A., Spiegel D. S., 2013, *MNRAS*, **431**, 621
 Park H., Shapiro P. R., Komatsu E., Iliev I. T., Ahn K., Mellema G., 2013, *ApJ*, **769**, 93
 Park H., Komatsu E., Shapiro P. R., Koda J., Mao Y., 2016, *ApJ*, **818**, 37
 Patil A. H., et al., 2017, *ApJ*, **838**, 65
 Planck Collaboration et al., 2014, *A&A*, **571**, A16

- Planck Collaboration et al., 2016, *A&A*, **596**, A108
 Shaw L. D., Rudd D. H., Nagai D., 2012, *ApJ*, **756**, 15
 Sunyaev R. A., Zeldovich I. B., 1980, *MNRAS*, **190**, 413
 Vishniac E. T., 1987, *ApJ*, **322**, 597
 Vrbanec D., et al., 2016, *MNRAS*, **457**, 666

This paper has been typeset from a $\text{\TeX}/\text{\LaTeX}$ file prepared by the author.